

BALM: Bundle Adjustment for Lidar Mapping

Zheng Liu and Fu Zhang

Abstract—We propose a framework for bundle adjustment (BA) on sparse lidar points and incorporate it to a lidar odometry and mapping (LOAM) to lower the drift. A local BA on a sliding window of keyframes has been widely used in visual SLAM and has proved to be very effective in lowering the drift. But in lidar mapping, BA method is hardly used because the sparse feature points (e.g., edge and plane) in a lidar point-cloud make the exact feature matching impossible. Our method is to enforce feature points lie on the same edge or plane by minimizing the eigenvalue of the covariance matrix. To speedup the optimization, we derive the analytical derivatives, up to second order, in closed form. Moreover, we propose a novel adaptive voxelization method to search feature correspondence efficiently. The proposed formulations are incorporated into a LOAM back-end for map refinement. Results show that, although as a back-end, the local BA can be solved very efficiently, even in real-time at 10Hz when optimizing 20 scans of point-cloud. The local BA also considerably lowers the LOAM drift. Our implementation of the BA optimization and LOAM are open-sourced to benefit the community¹.

I. INTRODUCTION

Bundle adjustment (BA) is the problem of jointly solving the 3D structures (i.e., location of feature points) and camera poses [1] and it has been an basic problem in various visual applications, such as structure from motion (SfM) [2], visual SLAM (simultaneous localization and mapping) [3], and visual-inertial navigation [4, 5].

Similar bundle adjustment can be defined for lidar mapping where the goal is to jointly determine the lidar pose and the global 3D point-cloud map. This would be a key problem in lowering the drift in lidar SLAM. Constrained by the pairwise matching nature of existing scan registration methods, such as iterative closest points (ICP) [6], generalized ICP [7], normal distribution transform [8], and surfel-based registration [9], commonly used lidar navigation and mapping (LOAM) framework [10] and its variants [11, 12] usually build the map by incrementally registering new scans. Such an incremental mapping process would accumulate registrations errors very quickly, especially in featureless environments where degeneration occurs [13] or for lidars of small FoV [12]. One way to lower such drift is performing a local BA over a sliding window of lidar scans, which allows us to re-assess the past scans based on new information in the following scans. This method has been widely used in visual navigation and proved to be very effective [4, 5].

While lidar BA seems simpler than visual BA due to the direct depth measurements, its formulation is actually more complicated. In visual BA, the measurements are high-resolution images where each pixel corresponds to a single

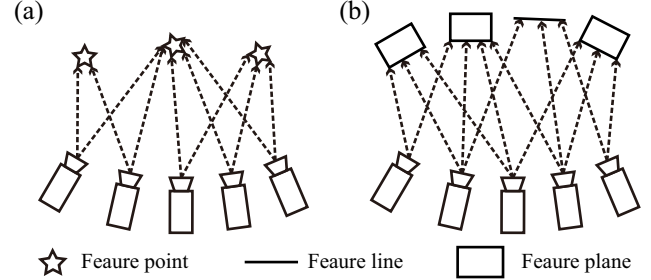


Fig. 1. Comparison of BA formulations: (a) visual BA constrains feature points to locate at the same point; (b) our proposed lidar BA constrains feature points to lie on the same edge or plane.

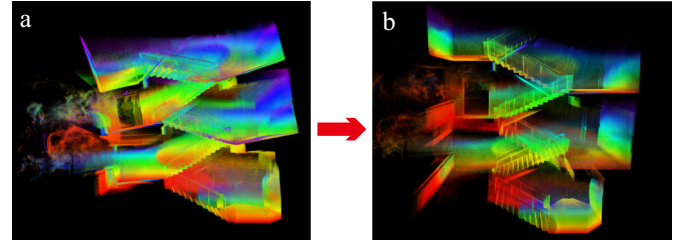


Fig. 2. (a) LOAM mapping without map refinement. (b) Refining the map using a local BA on a sliding window of lidar scans.

feature in the space in Fig. 1 (a). Hence, a natural formulation would be to minimize the difference between the projected feature location and its actual location on the image. However, this natural formulation does not apply to lidar: lidar point-cloud is usually very sparse and even non-repetitive [12], making the exact point matching infeasible.

In this paper, we propose a formulation of lidar BA and incorporate it into a LOAM framework as the back-end to refine the incrementally built map. More specifically, our contribution is as follows: 1) We propose a theoretical framework to perform lidar BA. Unlike visual BA which constrains the feature's exact location, our method constrains feature points to lie on the same line or plane (see Fig. 1 (b)) by minimizing the eigenvalues of the point covariance matrix. To enable efficient BA, we analytically derive the gradient and Hessian matrix of the cost function (i.e., eigenvalues) with respect to the scan poses; 2) We propose an adaptive voxelization to search for feature correspondence efficiently; and 3) We incorporate the proposed lidar BA into a LOAM back-end for map refinement and demonstrated its effectiveness on both spinning lidars and lidars of small FoV (e.g., Livox Horizon²) by comparing with existing LOAM implementations shown in Fig 2. Results show that the local BA effectively lowers the drift. Although it is designed as a back-end, the local BA runs very fast: when optimizing a sliding window of 20

Z. Liu and F. Zhang are with the Department of Mechanical Engineering, University of Hong Kong, Hong Kong, China. u3007335@connect.hku.hk, fuzhang@hku.hk

¹<https://github.com/hku-mars/BALM>

²<https://www.livoxtech.com/horizon>

scans, it runs nearly real-time at 10Hz. The BA formulation, optimization libraries, and LOAM implementations are open-sourced to the community.

II. RELATED WORK

Our definition of the lidar BA is most similar to the multi-view registration. Early work in this direction [14, 15] directly extend the ICP method [6] to the multi-scans cases, where the cost function is the sum of all distance between two corresponding points in any two scans. Similarly, Neugebauer [16] uses the distance between two corresponding surfaces in any two scans. While these methods work well for dense 3D scans (e.g., depth camera), they all require exact point or surface matching that seldom exists in lidar point-cloud.

The work in [17]–[23] register any two scans sharing overlaps using standard pairwise scan registration methods. Then the obtained relative poses are used as measurements to construct a pose graph, from which the poses can be solved by graph optimization. These methods require to perform repeated pairwise scan registration among scans having all the same overlaps. Moreover, it does not optimize the point map directly, restricting the attainable level of mapping consistency.

The difficulty of lidar BA (or multi-view registration) lies in defining a metric that effectively evaluates the alignment quality of sparse points from all scans and, in the meantime, allows efficient optimization. The correlation (or entropy)-based scan registration in [24] naturally extends to multiple scans, however, it requires to compute the correlation between all point pairs, a computation-costly procedure that requires careful engineering [25] or GPU acceleration [26]. More recently, Ferrer [27] evaluates the point quality by eigenvalues similar to our method. However, the method in [27] only uses the gradient information and the resultant optimization is very inefficient. In contrast, we analytically derived the derivatives, up to second order, which enables efficient even real-time optimization.

There are also some existing work on LOAM with sliding window optimization. Ye *et al.* [28] optimize a sliding window of lidar scans by registering each scan in the sliding window to the map built so far. This essentially ignored all constraints among scans within the sliding window, hence leads to sub-optimal solutions. Accounting for all these constraints would lead to repeated pairwise scan registration as in [29]. Droschel *et al.* [30] uses a multi-resolution occupancy grid map which allows multi-view registration but is too costly in memory or computation [31]. Compared to these work, our method considers constraints among all scans either in the sliding window or from the map and can be solved very efficiently.

The rest of the paper is organized as follows: In Section III, we present the theoretical framework for BA on sparse lidar points. The adaptive voxelization is presented in Section IV. We present our LOAM implementation with a local BA in Section V. The experiments are detailed in Section VI. Finally, Section VII concludes the paper and presents future work.

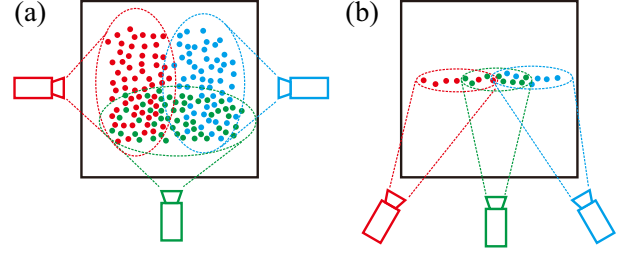


Fig. 3. A feature in space and the corresponding feature points drawn from multiple scans: (a) plane feature; (b) edge feature.

III. BA FORMULATION AND DERIVATIVES

A. Problem formulation

Given a group of sparse feature points \mathbf{p}_{f_i} ($i = 1, \dots, N$) drawn from M scans but all correspond to the same feature, either plane or edge (see Fig. 3). Assume the i -th feature point is drawn from the s_i -th scan, where $i \in \{1, \dots, N\}$ and $s_i \in \{1, \dots, M\}$, and denote pose of the M scans as $\mathbf{T} = (\mathbf{T}_1, \dots, \mathbf{T}_M)$, where $\mathbf{T}_j = (\mathbf{R}_j, \mathbf{t}_j) \in SO(3) \times \mathbb{R}^3$ and $j \in \{1, \dots, M\}$. Then, the feature point in global frame is

$$\mathbf{p}_i = \mathbf{R}_{s_i} \mathbf{p}_{f_i} + \mathbf{t}_{s_i}; \quad i = 1, \dots, N. \quad (1)$$

As defined previously, the problem of lidar BA refers to jointly determining the poses of the M scans and the global 3D point-cloud map. Now the 3D map is a single feature (edge or plane), then the BA reduces to jointly determining the poses \mathbf{T} and location of the single feature, which is represented by a point \mathbf{q} on the feature and a unit vector \mathbf{n} (\mathbf{n} is the normal vector of the plane or the direction of the edge). In case of plane feature, the direct BA formulation is to minimize the distance from each plane feature point \mathbf{p}_i , which depends on the pose \mathbf{T}_{s_i} , to the plane:

$$(\mathbf{T}^*, \mathbf{n}^*, \mathbf{q}^*) = \arg \min_{\mathbf{T}, \mathbf{n}, \mathbf{q}} \frac{1}{N} \sum_{i=1}^N (\mathbf{n}^T (\mathbf{p}_i - \mathbf{q}))^2 \quad (2)$$

$$= \arg \min_{\mathbf{T}} \underbrace{\left(\min_{\mathbf{n}, \mathbf{q}} \frac{1}{N} \sum_{i=1}^N (\mathbf{n}^T (\mathbf{p}_i - \mathbf{q}))^2 \right)}_{=\lambda_3(\mathbf{A}); \text{ when } \mathbf{n}=\mathbf{u}_3, \mathbf{q}=\bar{\mathbf{p}}} \quad (3)$$

where $\lambda_3(\mathbf{A})$ denotes the minimal eigenvalue of matrix \mathbf{A} , \mathbf{u}_3 is the corresponding eigenvector, $\bar{\mathbf{p}}$ and \mathbf{A} are:

$$\bar{\mathbf{p}} = \frac{1}{N} \sum_{i=1}^N \mathbf{p}_i; \quad \mathbf{A} = \frac{1}{N} \sum_{i=1}^N (\mathbf{p}_i - \bar{\mathbf{p}}) (\mathbf{p}_i - \bar{\mathbf{p}})^T. \quad (4)$$

Equation (3) implies that the optimal feature location and normal can be written as a function of the poses \mathbf{T} , hence the optimization need only to be performed on the latter. This agrees well to our intuition that as long as the scan pose is determined, the 3D point-cloud map. Moreover, the optimization on the scan poses \mathbf{T} reduces to minimizing the minimal eigenvalues λ_3 of the point covariance matrix \mathbf{A} defined in (4).

Mimicking the plane feature, the cost for an edge feature is the second minimal eigenvalue λ_2 of the point covariance matrix (4). In sum, the lidar BA minimizes the sum of many cost items, each is in the following form

$$\lambda_k(\mathbf{p}(\mathbf{T})), \quad (5)$$

where $\mathbf{p} = [\mathbf{p}_1^T \cdots \mathbf{p}_n^T]^T$ is the vector of all feature points corresponding to the same feature.

To allow efficient optimization with the cost in (5), we analytically derive the closed-form derivatives, up to second order, with respect to the pose \mathbf{T} . Due to the chain rule, we derive the derivatives with respect to the point vector \mathbf{p} first.

B. The Derivatives

Theorem 1. For a group of points, \mathbf{p}_i ($i = 1, \dots, N$) and the covariance matrix \mathbf{A} defined in (4). Assume \mathbf{A} has eigenvalues λ_k corresponding to eigenvectors \mathbf{u}_k ($k = 1, 2, 3$), then

$$\frac{\partial \lambda_k}{\partial \mathbf{p}_i} = \frac{2}{N} (\mathbf{p}_i - \bar{\mathbf{p}})^T \mathbf{u}_k \mathbf{u}_k^T, \quad (6)$$

where the $\bar{\mathbf{p}}$ is the average of the N points as in (4).

Theorem 2. For a group of points, \mathbf{p}_i ($i = 1, \dots, N$) and the covariance matrix \mathbf{A} defined in (4). Assume \mathbf{A} has eigenvalues λ_k corresponding to eigenvectors \mathbf{u}_k ($k = 1, 2, 3$). Moreover, $\lambda_i \neq \lambda_k$ when $i \neq k$, then

$$\frac{\partial^2 \lambda_k}{\partial \mathbf{p}_j \partial \mathbf{p}_i} = \begin{cases} \frac{2}{N} \left(\frac{N-1}{N} \mathbf{u}_k \mathbf{u}_k^T + \mathbf{u}_k (\mathbf{p}_i - \bar{\mathbf{p}})^T \mathbf{U} \mathbf{F}_k^{\mathbf{p}_j} + \mathbf{U} \mathbf{F}_k^{\mathbf{p}_j} (\mathbf{u}_k^T (\mathbf{p}_i - \bar{\mathbf{p}})) \right), & i = j \\ \frac{2}{N} \left(-\frac{1}{N} \mathbf{u}_k \mathbf{u}_k^T + \mathbf{u}_k (\mathbf{p}_i - \bar{\mathbf{p}})^T \mathbf{U} \mathbf{F}_k^{\mathbf{p}_j} + \mathbf{U} \mathbf{F}_k^{\mathbf{p}_j} (\mathbf{u}_k^T (\mathbf{p}_i - \bar{\mathbf{p}})) \right), & i \neq j \end{cases} \quad (7)$$

$$\mathbf{F}_k^{\mathbf{p}_j} = \begin{bmatrix} \mathbf{F}_{1,k}^{\mathbf{p}_j} \\ \mathbf{F}_{2,k}^{\mathbf{p}_j} \\ \mathbf{F}_{3,k}^{\mathbf{p}_j} \end{bmatrix} \in \mathbb{R}^{3 \times 3}, \quad \mathbf{U} = [\mathbf{u}_1 \quad \mathbf{u}_2 \quad \mathbf{u}_3],$$

$$\mathbf{F}_{m,n}^{\mathbf{p}_j} = \begin{cases} \frac{(\mathbf{p}_j - \bar{\mathbf{p}})^T}{N(\lambda_n - \lambda_m)} (\mathbf{u}_m \mathbf{u}_n^T + \mathbf{u}_n \mathbf{u}_m^T), & m \neq n \\ \mathbf{0}_{1 \times 3}, & m = n \end{cases}$$

C. Second order approximation

With the first and second order derivatives in previous sections, we can approximate the cost function (5) by its second order approximation as below:

$$\lambda_k(\mathbf{p} + \delta \mathbf{p}) = \lambda_k(\mathbf{p}) + \mathbf{J}(\mathbf{p}) \delta \mathbf{p} + \frac{1}{2} \delta \mathbf{p} \mathbf{H}(\mathbf{p}) \delta \mathbf{p}, \quad (8)$$

where $\mathbf{J}(\mathbf{p})$ is the Jacobian matrix with i -th elements in (6) and $\mathbf{H}(\mathbf{p})$ is the Hessian matrix with i -th row, j -th column elements in (7).

Recall that the point vector \mathbf{p} is further dependent on the scan poses \mathbf{T} as in (1). Perturbing a pose \mathbf{T}_j in its tangent

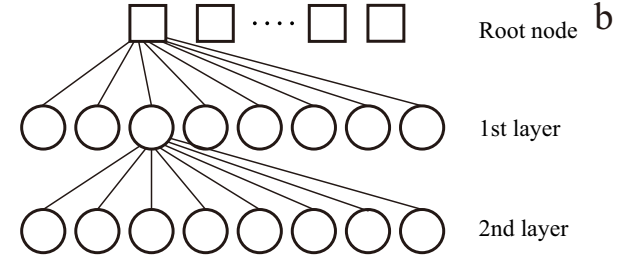
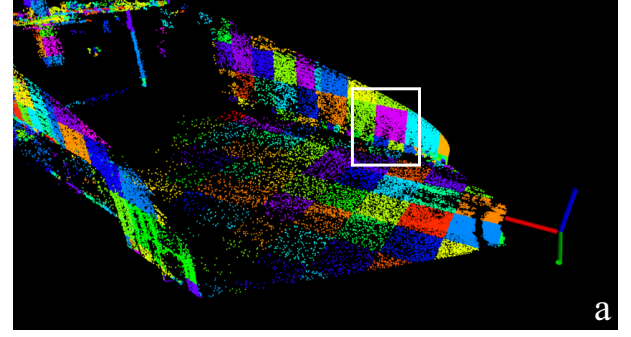


Fig. 4. (a) An exemplary voxel map, different color represents different voxels, which may have different size (e.g., voxels in the white box). (b) All octrees are indexed in a Hash table.

plane $\delta \mathbf{T}_j = [\phi_j^T \quad \delta \mathbf{t}_j^T]^T$ using the \boxplus operation defined in [32], we have

$$\mathbf{T}_j = (\mathbf{R}_j, \mathbf{t}_j); \quad \mathbf{T}_j \boxplus \delta \mathbf{T}_j = (\mathbf{R}_j \exp(\phi_j^\wedge), \mathbf{t}_j + \delta \mathbf{t}_j) \quad (9)$$

and

$$\mathbf{p}_i = \mathbf{R}_{s_i} \exp(\phi_{s_i}^\wedge) \mathbf{p}_{f_i} + \mathbf{t}_{s_i}; \quad \frac{\delta \mathbf{p}_i}{\delta \mathbf{T}_{s_i}} = [-\mathbf{R}_{s_i} (\mathbf{p}_{f_i})^\wedge \quad \mathbf{I}] \quad (10)$$

$$\mathbf{D} = \frac{\delta \mathbf{p}}{\delta \mathbf{T}} = \begin{bmatrix} \vdots & & \\ \cdots & \mathbf{D}_{ij} & \cdots \\ \vdots & & \end{bmatrix} \in \mathbb{R}^{3N \times 6M} \quad (11)$$

$$\mathbf{D}_{ij} = \begin{cases} \frac{\delta \mathbf{p}_i}{\delta \mathbf{T}_{s_i}} & \text{for } j = s_i \in \{1, \dots, M\} \\ \mathbf{0}_{3 \times 6} & \text{for else} \end{cases} \quad (12)$$

Substituting (12) into (8) leads to

$$\lambda_k(\mathbf{T} \boxplus \delta \mathbf{T}) = \lambda_k(\mathbf{T}) + \underbrace{\mathbf{J} \mathbf{D}}_{\mathbf{J}} \delta \mathbf{T} + \frac{1}{2} \delta \mathbf{T} \underbrace{\mathbf{D}^T \mathbf{H} \mathbf{D}}_{\bar{\mathbf{H}}} \delta \mathbf{T}. \quad (13)$$

Finally, we use a Levenberg-Marquardt (LM) [33] method to minimize the cost λ_k by repeatedly approximating it by the second order approximation (13). In each iteration, the solution is solved from

$$(\bar{\mathbf{H}}(\mathbf{p}) + \mu \mathbf{I}) \delta \mathbf{p}^* = -\bar{\mathbf{J}}(\mathbf{p})^T, \quad (14)$$

where μ is the stepsize determined from the LM method.

IV. ADAPTIVE VOXELIZATION

The BA formulation in Section. III requires to find all feature points corresponding to the same feature (edge or plane). To do so, we propose a novel adaptive voxelization method: assume that a rough initial pose of different scans

are available (e.g., from a LOAM odometry), we repeatedly voxelizing the 3D space from a default size (e.g., $1m$): if all feature points (from all scans) in the current voxel lie on a plane or edge (e.g., by examining the eigenvalue of the point covariance matrix (4)), the current voxel is kept in memory along with the contained feature points; otherwise, the current voxel breaks into eight octants and proceeds to check each octant until reaching the minimal size. The proposed adaptive voxelization generates a voxel map, where different voxels may have different size adapted to the environment. For each voxel, it corresponds to one feature, and hence one cost item as in (13). An exemplary voxel map is seen in Fig. 4 (a).

The adaptive voxelization has many advantages: 1) It is naturally compatible with existing data structures such as octrees, hence its implementation and efficiency can be greatly facilitated; 2) It is usually more efficient than constructing a full octree on feature points [10] as early termination may occur when the contained feature points lie on the same plane or edge. Such an advantage will be more obvious when the environment has large planes or long edges; 3) A map with adaptive voxels will lower the time for searching feature correspondences in lidar odometry. It is only necessary to search the voxel a feature point lies in or near to, instead of the nearest points that require more exhaustive search [10].

In our implementation, we construct two voxel maps, one for edge features and one for planar features. The voxel map, by its construction, naturally suits to an octree structure. To reduce the depth of the octree, we use a set of octrees indexed by a Hash table (see Fig. 4 (b)). Each octree corresponds a non-empty cube of the default voxel size (e.g., $1m$) in the space. Different octrees may have different depth, depending on the geometry of that cube in the space. Each leaf node (i.e., a voxel) in an octree saves feature points all corresponding to the same feature (e.g., plane or edge).

Remark 1. If a voxel contains too many points, the Hessian matrix in (8) would have high dimension, in this case, we could average the points from the same scan. The averaged points have fewer number and lie on the same plane determined by the raw feature points. This allows to save much computation with degrading the mapping consistency.

Remark 2. The Hessian matrix computed in Theorem 2 requires $\lambda_i \neq \lambda_k$ when $i \neq k$. For a voxel whose λ_k has multiplicity more than one, we simply leave out it.

Remark 3. Although we keep saying edge features and plane features, the method naturally extends to non-planar features (e.g., curved surfaces) by constructing the voxel map at a finer level and allowing larger variance when examining whether the contained points lie on the same plane.

V. LOAM WITH LOCAL BA

In this section, we incorporate the proposed BA formulation and its optimization methods into a LOAM framework. The system overview is shown in Fig. 5. It consists of three parallel threads: feature extraction, odometry, and map-refinement. The feature extraction thread extracts the edge and plane features similar to [10] and [12].

Once receiving a new scan of feature points, the odometry estimates the lidar pose by registering the new scan to the

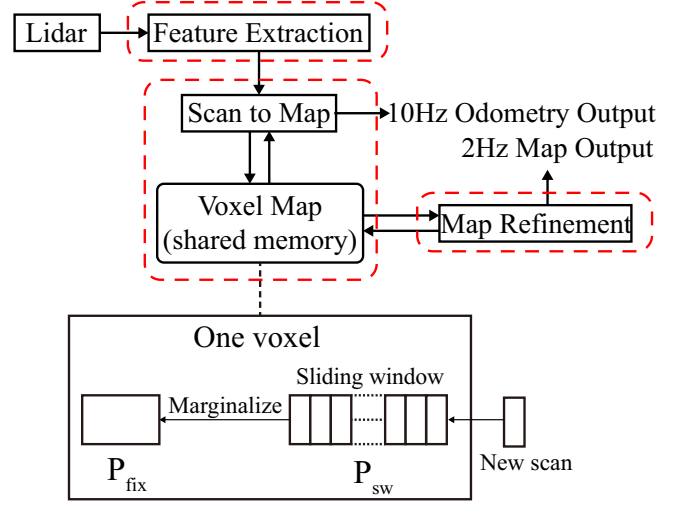


Fig. 5. Overview of LOAM with local BA.

existing map. Unlike the existing methods [10, 12] where each feature point is matched to some nearest points in the map, we leverage the adaptive voxel map to speedup the matching process. More specifically, when constructing the voxel map, we compute the center point and normal (or direction) vector of the plane (or edge) in a voxel. Then for a point in the new scan, we search the nearest voxel (represented by its center point) and compute the distance between the point and the plane or edge feature in the voxel.

With the odometry, the new scan can be roughly registered to the global frame and be pushed to the voxel map: for each point in the new scan, search the voxel it lies in and add this point to the leaf node of the corresponding octree. If no voxel is found in the existing map for the point in the new scan, create a new octree, index its root in the Hash table, and add this point to the root node. After all feature points of the new scan are distributed to the leaf node of existing octrees or the root node of newly created octrees, we update the voxel map as the way it is constructed: if points in a node (leaf or node) do not make a single feature (plane or edge), divide the node into eight and check each of them.

After pushing a certain number of new scans to the voxel map, a map-refinement is triggered. The map-refinement performs a local BA on a sliding window of lidar poses. Any voxel containing points within the sliding window (i.e., P_{sw}) are used to construct cost items as (5). Then, the map-refinement repeatedly minimizes the second order approximation (13) of the total cost consisting of all relevant voxels. This refines all the lidar poses within the sliding window. The updated poses are then used to update the center points and normal vectors of all involved voxels.

Once the sliding window is full, points from older scans are merged to the map points P_{fix} . A nice property of the point covariance matrix (4) is the existence of recursive form [34], allowing all points outside the sliding window to be summarized in a few compact matrices and vectors without saving the raw points (see lower part of Fig. 5). The merged points P_{fix} will be retained in the voxel map for odometry

and map-refinements.

VI. EXPERIMENTS

We present experimental results to verify the effectiveness of the proposed BA in LOAM. In the experiment, the lidar odometry runs a 10Hz, the map-refinement is triggered after receiving 5 scans hence running at 2Hz. We use a sliding window of 20 most recent scans. All the experiments run on a laptop computer with CPU i7-10750H and 16Gib memory. The algorithm is implemented in C++ and executed in the robot operating system (ROS) [35] with Ubuntu Linux and PCL 1.7 [36].

A. Parking lot

We test our algorithm in a medium size parking lot on a Livox Horizon lidar, which has a $25^\circ \times 82^\circ$ FoV, and compare its performance with that of a state-of-art implementation of LOAM [10] for the Livox Horizon lidar³.

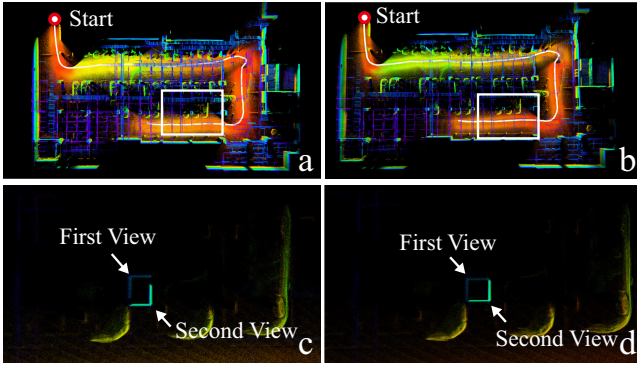


Fig. 6. Experiment 1 of parking lot: (a) and (c) are results from LOAM, (b) and (d) are from our method, BALM

1) *Experiment 1*: In this experiment, the lidar is fixed on a small UGV. The maps are shown in Fig. (a) and Fig. (b) built by LOAM and BALM, respectively. As shown by its path (the white curve), the lidar can see a pillar (the white boxes) at two times. Every time two sides of the pillar are observed and the pillar should be a closed rectangle in the map if no drift exists. Zooming out the pillar part contained in the white box of Fig. 6 (a), Fig.6 (c) shows that the pillar is not closed. In contrast, in Fig. (d) obtained by BALM, the pillar is well closed. When the UGV takes two turns and sees the pillar for the second time, the drift is accumulated in yaw angle for LOAM algorithm. Our method optimizes 20 scans together in a sliding window so the drift is reduced significantly.

2) *Experiment 2*: In this experiment, the lidar is handheld and moving in underground parking lot with slopes. The scene can be seen in Fig. 7 (a) and the path is the white line. The scene contains two challenging slopes which can be seen in the Fig. 7 (a) and (b) and will cause drift on the Z-axis for lidar odometry. The starting and end positions are at the same height but not the same position (although very close to each other) limited by the actual collection process. The mapping results around the start/end point is shown in the Fig. 7 (c)

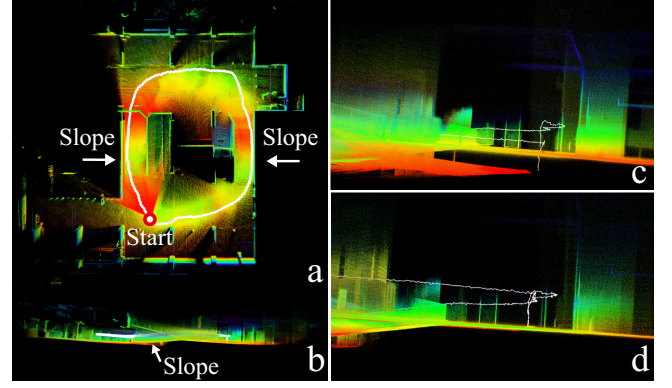


Fig. 7. Experiment 2 of parking lot: (a) the overall scene, (b) a slope in the scene, (c) and (d) show the map and odometry (white line) results around start/end position of LOAM and our method BALM, respectively.

TABLE I
DRIFT OF EXPERIMENT 2.

Distance(84m)	LOAM (cm)	BALM (cm)
Translation error	79.7 (0.94%)	5.8 (0.07%)

and Fig. 7 (d) obtained from LOAM and BALM, respectively. It is seen that the drift of BALM is much lower than LOAM. The translation error is listed in Table I.

B. Indoor

In this experiment, we test our algorithm on Livox Mid-40 lidars⁴ and compare its performance with LOAM implementation³. The lidar is placed on a UGV and moves in an indoor office area. For a classic 360° spinning lidar, it is easy to take turns in a corridor. But for the Livox Mid-40 lidar with a small 40° FoV, degeneration occurs easily because of the lessen feature points. Fig. 8 (a) shows overview of the area and the turn is framed by a white rectangle. In Fig. 8 (b), the odometry of LOAM is “raised” because of few feature points. The map can be seen in Fig. (d). For BALM, future scans is used to ensure the pose of a scan and more feature points can be used. Hence, the odometry in Fig. 8 (c) is more stable. The overall map in Fig. (e) is also more consistent than the LOAM in Fig. (d).

C. Outdoor

We further test our algorithm on Velodyne VLP-16 lidar. We use the data offered by LeGO-LOAM [11] available on Github⁵, and perform comparison study. The path has the same starting and end point. The scene can be seen in Fig. 9 (a) and the path is colored in white. The paths of LOAM, LeGO-LOAM and BALM are shown in Fig.9 (b). The drift when returning to start is given in Table II.

D. Running time

In LOAM, a feature point in new scan should find five closest points, but in BALM, the feature point just need to find

³https://github.com/Livox-SDK/livox_mapping

⁴<https://www.livoxtech.com/mid-40-and-mid-100>

⁵<https://github.com/RobustFieldAutonomyLab/LeGO-LOAM>

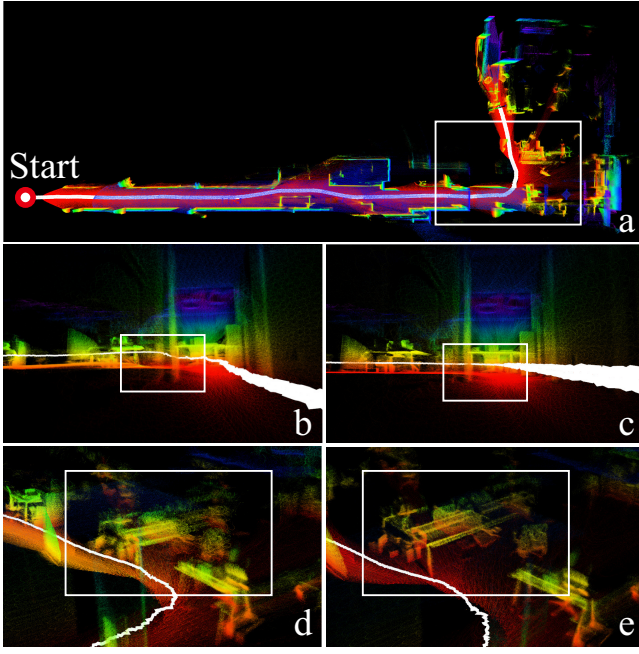


Fig. 8. Indoor mapping and odometry results: (a) the overall scene; (b) and (d) show the odometry and mapping results of LOAM; (c) and (e) show our method BALM.

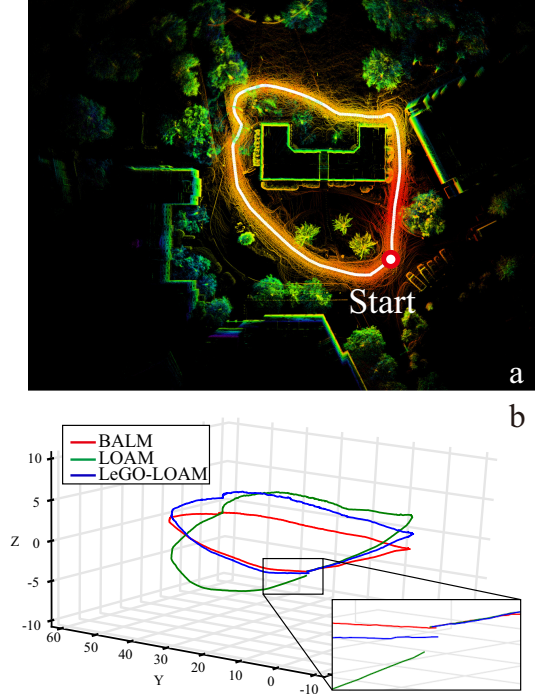


Fig. 9. Outdoor mapping and odometry results. (a) The overview of the scene; (b) The paths of LOAM, LeGO-LOAM and BALM

closest voxel (plane or edge), which can reduce the searching time in the scan to map. The comparison is shown in Fig. 10(a) where the running time is for building kd-tree, finding closed points/voxels and LM optimization. The data of running time is obtained by experiment A, B and C. To make a fair comparison, a fixed two-step L-M optimization is used for both methods.

TABLE II
DRIFT OF THE OUTDOOR SCENE.

Distance(210m)	LOAM (cm)	LeGO-LOAM (cm)	BALM (cm)
Translation error	56.8 (0.27%)	38.5 (0.18%)	28.0 (0.13%)

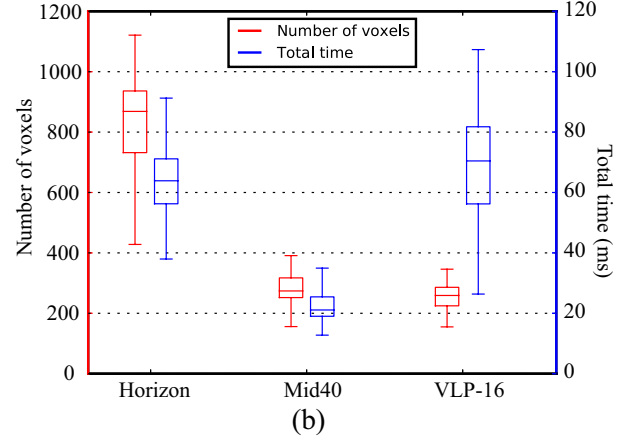
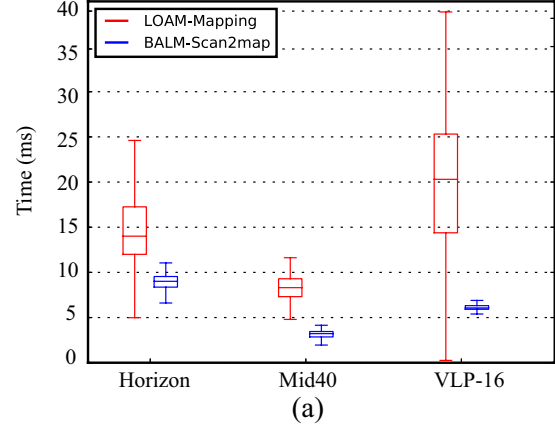


Fig. 10. Running time: (a) scan to map; (b) local BA.

Finally, Fig. 10(b) shows the number of voxels for a sliding window of 20 most recent scans and the time for local BA and voxel map update. It is seen that in most cases, the local BA and voxel map update can complete in 100ms. This implies that the local BA can nearly run at the same frequency as the odometry (i.e., 10Hz), able to run nearly at the odometry leading to nearly real-time performance.

VII. CONCLUSION AND FUTURE WORKS

This paper formulated a a framework for lidar bundle adjustment (BA) and developed theoretical derivatives allowing efficient optimization. A novel adaptive voxelization is proposed to support the lidar BA. Then the proposed BA and optimization methods are further incorporated into a LOAM framework to serve as the back-end for map refinement. Experiments on various lidars and environments validate the effectiveness of the proposed methods.

The current implementation of local BA in LOAM uses a sliding window of temporal scans, leading to redundant information in adjacent scans sharing large overlaps. Moreover, it uses a simple scan-to-map front-end without compensating

any motion distortion or leveraging any motion model. Future works will adopt keyframes in a local sliding window and further incorporate motion models. Besides the LOAM, the proposed BA can also be used for global mapping and extrinsic calibration, which will also be explored in the future.

APPENDIX A

A. Proof of theorem 1

Denote a point $\mathbf{p}_i = [x_i \ y_i \ z_i]^T$ and the eigenvector matrix $\mathbf{U} = [\mathbf{u}_1 \ \mathbf{u}_2 \ \mathbf{u}_3]^T$. Further denote p an element of \mathbf{p}_i , p is one of x_i, y_i and z_i . Then by definition, we have

$$\mathbf{\Lambda} = \mathbf{U}^T \mathbf{A} \mathbf{U} \quad (15)$$

$$\frac{\partial \mathbf{\Lambda}}{\partial p} = \left(\frac{\partial \mathbf{U}}{\partial p} \right)^T \mathbf{A} \mathbf{U} + \mathbf{U}^T \frac{\partial \mathbf{A}}{\partial p} \mathbf{U} + \mathbf{U}^T \mathbf{A} \frac{\partial \mathbf{U}}{\partial p} \quad (16)$$

$$\mathbf{U}^T \mathbf{A} = \mathbf{\Lambda} \mathbf{U}^T; \mathbf{A} \mathbf{U} = \mathbf{U} \mathbf{\Lambda} \quad (17)$$

Plugging (17) into (16) yields:

$$\frac{\partial \mathbf{\Lambda}}{\partial p} = \mathbf{U}^T \frac{\partial \mathbf{A}}{\partial p} \mathbf{U} + \underbrace{\mathbf{\Lambda} \mathbf{U}^T \frac{\partial \mathbf{U}}{\partial p}}_{(\mathbf{C}^p)^T} + \underbrace{\left(\frac{\partial \mathbf{U}}{\partial p} \right)^T \mathbf{U} \mathbf{\Lambda}}_{(\mathbf{C}^p)^T} \quad (18)$$

As $\mathbf{U}^T \mathbf{U} = \mathbf{I}$, where \mathbf{I} is the identity matrix, partial differentiating both sides with respect to p leads to

$$\mathbf{U}^T \frac{\partial \mathbf{U}}{\partial p} + \left(\frac{\partial \mathbf{U}}{\partial p} \right)^T \mathbf{U} = \mathbf{0} \implies \mathbf{C}^p + (\mathbf{C}^p)^T = \mathbf{0}.$$

It is seen that \mathbf{C}^p is a skew symmetric matrix whose diagonal elements are zeros. Moreover, since $\mathbf{\Lambda}$ is diagonal, the last two items of the right side of (18) sum to zero on diagonal positions. Only considering the diagonal elements in (18) leads to

$$\frac{\partial \lambda_k}{\partial p} = \mathbf{u}_k^T \frac{\partial \mathbf{A}}{\partial p} \mathbf{u}_k = \frac{\partial \mathbf{u}_k^T \mathbf{A} \mathbf{u}_k}{\partial p} \quad (k = 1, 2, 3)$$

where in the second equation the vector \mathbf{u}_k is viewed constant. Stacking the partial differentiation of λ_k with respect to all elements of \mathbf{p}_i leads to

$$\frac{\partial \lambda_k}{\partial \mathbf{p}_i} = \left[\frac{\partial \mathbf{u}_k^T \mathbf{A} \mathbf{u}_k}{\partial x_i} \quad \frac{\partial \mathbf{u}_k^T \mathbf{A} \mathbf{u}_k}{\partial y_i} \quad \frac{\partial \mathbf{u}_k^T \mathbf{A} \mathbf{u}_k}{\partial z_i} \right] = \frac{\partial \mathbf{u}_k^T \mathbf{A} \mathbf{u}_k}{\partial \mathbf{p}_i}$$

Recall the definition of matrix \mathbf{A} in (4) and that

$$\frac{\partial \mathbf{p}_j}{\partial \mathbf{p}_i} = \mathbf{I}, (i = j) \quad \frac{\partial \mathbf{p}_j}{\partial \mathbf{p}_i} = \mathbf{0}, (i \neq j),$$

Then, we can obtain

$$\begin{aligned} \frac{\partial \lambda_k}{\partial \mathbf{p}_i} &= \frac{1}{N} \sum_{j=1}^N \frac{\partial \mathbf{u}_k^T (\mathbf{p}_j - \bar{\mathbf{p}}) (\mathbf{p}_j - \bar{\mathbf{p}})^T \mathbf{u}_k}{\partial \mathbf{p}_i} \\ &= \frac{2}{N} \sum_{j=1}^N (\mathbf{p}_j - \bar{\mathbf{p}})^T \mathbf{u}_k \frac{\partial \mathbf{u}_k^T (\mathbf{p}_j - \bar{\mathbf{p}})}{\partial \mathbf{p}_i} \\ &= \frac{2}{N} (\mathbf{p}_i - \bar{\mathbf{p}})^T \mathbf{u}_k \mathbf{u}_k^T (\mathbf{I} - \frac{1}{N} \mathbf{I}) \\ &\quad + \frac{2}{N} \sum_{j=1, j \neq i}^N (\mathbf{p}_j - \bar{\mathbf{p}})^T \mathbf{u}_k \mathbf{u}_k^T (-\frac{1}{N} \mathbf{I}) \\ &= \frac{2}{N} (\mathbf{p}_i - \bar{\mathbf{p}})^T \mathbf{u}_k \mathbf{u}_k^T. \quad \blacksquare \end{aligned} \quad (19)$$

B. Proof of theorem 2

Consider two points, $\mathbf{p}_i = [x_i \ y_i \ z_i]^T$ and $\mathbf{p}_j = [x_j \ y_j \ z_j]^T$. Denote q a element of \mathbf{p}_j , q is one of x_j, y_j and z_j . Since the eigenvector matrix \mathbf{U} is orthogonal, so

$$\mathbf{U}^T \frac{\partial \mathbf{U}}{\partial q} + \left(\frac{\partial \mathbf{U}}{\partial q} \right)^T \mathbf{U} = \mathbf{0}$$

Define

$$\mathbf{C}^q = \mathbf{U}^T \frac{\partial \mathbf{U}}{\partial q}, \quad \mathbf{C}^q + (\mathbf{C}^q)^T = \mathbf{0}$$

The elements on the diagonal of \mathbf{C}^q is zero. Similarly with (18) and replace p with q

$$\frac{\partial \mathbf{\Lambda}}{\partial q} = \mathbf{U}^T \frac{\partial \mathbf{A}}{\partial q} \mathbf{U} + \mathbf{\Lambda} \mathbf{C}^q - \mathbf{C}^q \mathbf{\Lambda} \quad (20)$$

Since $\mathbf{\Lambda}$ is diagonal and hence $\frac{\partial \mathbf{\Lambda}}{\partial q}$, for off-diagonal elements in (20), we have

$$0 = \mathbf{u}_m^T \frac{\partial \mathbf{A}}{\partial q} \mathbf{u}_n + \lambda_m \mathbf{C}_{m,n}^q - \mathbf{C}_{m,n}^q \lambda_n$$

$\mathbf{C}_{m,n}^q$ is the m -th row and n -th column element in \mathbf{C}^q as below if $\lambda_m \neq \lambda_n$

$$\mathbf{C}_{m,n}^q = \begin{cases} \frac{1}{\lambda_n - \lambda_m} \mathbf{u}_m^T \frac{\partial \mathbf{A}}{\partial q} \mathbf{u}_n, & m \neq n \\ 0, & m = n \end{cases} \quad (21)$$

According the definition of \mathbf{C}^q ,

$$\frac{\partial \mathbf{u}_k}{\partial q} = \frac{\partial \mathbf{U} \mathbf{e}_k}{\partial q} = \mathbf{U} \mathbf{C}^q \mathbf{e}_k$$

where \mathbf{e}_k is a 3×1 vector in which the k -th element is 1 and the rests 0. Stacking the partial differentiation of \mathbf{u}_k with respect to all elements of \mathbf{p}_j leads to

$$\begin{aligned} \frac{\partial \mathbf{u}_k}{\partial \mathbf{p}_j} &= \begin{bmatrix} \frac{\partial \mathbf{U} \mathbf{e}_k}{\partial x_j} & \frac{\partial \mathbf{U} \mathbf{e}_k}{\partial y_j} & \frac{\partial \mathbf{U} \mathbf{e}_k}{\partial z_j} \end{bmatrix} \\ &= [\mathbf{U} \mathbf{C}^{x_j} \mathbf{e}_k \quad \mathbf{U} \mathbf{C}^{y_j} \mathbf{e}_k \quad \mathbf{U} \mathbf{C}^{z_j} \mathbf{e}_k] \\ &= \mathbf{U} [\mathbf{C}^{x_j} \mathbf{e}_k \quad \mathbf{C}^{y_j} \mathbf{e}_k \quad \mathbf{C}^{z_j} \mathbf{e}_k] \\ &= \mathbf{U} \begin{bmatrix} \mathbf{C}_{1,k}^{x_j} & \mathbf{C}_{1,k}^{y_j} & \mathbf{C}_{1,k}^{z_j} \\ \mathbf{C}_{2,k}^{x_j} & \mathbf{C}_{2,k}^{y_j} & \mathbf{C}_{2,k}^{z_j} \\ \mathbf{C}_{3,k}^{x_j} & \mathbf{C}_{3,k}^{y_j} & \mathbf{C}_{3,k}^{z_j} \end{bmatrix} \end{aligned} \quad (22)$$

Define

$$\mathbf{F}_{m,n}^{\mathbf{p}_j} = [\mathbf{C}_{m,n}^{x_j} \quad \mathbf{C}_{m,n}^{y_j} \quad \mathbf{C}_{m,n}^{z_j}] \in \mathbb{R}^{1 \times 3}, \quad m, n \in \{1, 2, 3\}.$$

Then, stacking each element $\mathbf{C}_{m,n}^{x_j}$ as in (21) leads to

$$\mathbf{F}_{m,n}^{\mathbf{p}_j} = \begin{cases} \frac{1}{\lambda_n - \lambda_m} \frac{\partial \mathbf{u}_m^T \mathbf{A} \mathbf{u}_n}{\partial \mathbf{p}_j}, & m \neq n \\ \mathbf{0}, & m = n \end{cases}$$

where the vector \mathbf{u}_m and \mathbf{u}_n are viewed constant.

By derivations similar method in (19), we can further obtain the specific form of $\mathbf{F}_{m,n}^{\mathbf{p}_j}$, as follows:

$$\mathbf{F}_{m,n}^{\mathbf{p}_j} = \begin{cases} \frac{(\mathbf{p}_j - \bar{\mathbf{p}})^T}{N(\lambda_n - \lambda_m)} (\mathbf{u}_m \mathbf{u}_n^T + \mathbf{u}_n \mathbf{u}_m^T), & m \neq n \\ \mathbf{0}, & m = n \end{cases}$$

And hence (22) becomes

$$\frac{\partial \mathbf{u}_k}{\partial \mathbf{p}_j} = \mathbf{U} \begin{bmatrix} \mathbf{F}_{1,k}^{\mathbf{p}_j} \\ \mathbf{F}_{2,k}^{\mathbf{p}_j} \\ \mathbf{F}_{3,k}^{\mathbf{p}_j} \end{bmatrix} = \mathbf{U} \mathbf{F}_k^{\mathbf{p}_j} \quad (23)$$

With $\frac{\partial \lambda_k}{\partial \mathbf{p}_i}$ in (19) and $\frac{\partial \mathbf{u}_k}{\partial \mathbf{p}_j}$ in (23), we have:

$$\begin{aligned} \frac{\partial}{\partial \mathbf{p}_j} \left(\frac{\partial \lambda_k}{\partial \mathbf{p}_i} \right) &= \frac{2}{N} \left(\mathbf{u}_k \mathbf{u}_k^T \frac{\partial (\mathbf{p}_i - \bar{\mathbf{p}})}{\partial \mathbf{p}_j} + \mathbf{u}_k (\mathbf{p}_i - \bar{\mathbf{p}})^T \frac{\partial \mathbf{u}_k}{\partial \mathbf{p}_j} \right. \\ &\quad \left. + \frac{\partial \mathbf{u}_k}{\partial \mathbf{p}_j} \left(\mathbf{u}_k^T (\mathbf{p}_i - \bar{\mathbf{p}}) \right) \right) \\ &= \frac{2}{N} \left(\mathbf{u}_k \mathbf{u}_k^T \frac{\partial (\mathbf{p}_i - \bar{\mathbf{p}})}{\partial \mathbf{p}_j} + \mathbf{u}_k (\mathbf{p}_i - \bar{\mathbf{p}})^T \mathbf{U} \mathbf{F}_k^{\mathbf{p}_j} \right. \\ &\quad \left. + \mathbf{U} \mathbf{F}_k^{\mathbf{p}_j} \left(\mathbf{u}_k^T (\mathbf{p}_i - \bar{\mathbf{p}}) \right) \right) \quad (24) \end{aligned}$$

It should be noted that $\mathbf{u}_k (\mathbf{p}_i - \bar{\mathbf{p}})^T$ is a matrix but $\mathbf{u}_k^T (\mathbf{p}_i - \bar{\mathbf{p}})$ is a scalar. What is more,

$$\frac{\partial (\mathbf{p}_i - \bar{\mathbf{p}})}{\partial \mathbf{p}_j} = \begin{cases} \frac{N-1}{N} \mathbf{I}, & i = j \\ -\frac{1}{N} \mathbf{I}, & i \neq j \end{cases}$$

Therefore, (24) can be rewritten as (7). ■

REFERENCES

- [1] B. Triggs, P. F. McLauchlan, R. I. Hartley, and A. W. Fitzgibbon, "Bundle adjustment—a modern synthesis," in *International workshop on vision algorithms*. Springer, 1999, pp. 298–372.
- [2] S. Agarwal, N. Snavely, S. M. Seitz, and R. Szeliski, "Bundle adjustment in the large," in *European conference on computer vision*. Springer, 2010, pp. 29–42.
- [3] R. Mur-Artal, J. M. M. Montiel, and J. D. Tardos, "Orb-slam: a versatile and accurate monocular slam system," *IEEE transactions on robotics*, vol. 31, no. 5, pp. 1147–1163, 2015.
- [4] A. I. Mourikis and S. I. Roumeliotis, "A multi-state constraint kalman filter for vision-aided inertial navigation," in *Proceedings 2007 IEEE International Conference on Robotics and Automation*. IEEE, 2007, pp. 3565–3572.
- [5] S. Leutenegger, S. Lynen, M. Bosse, R. Siegwart, and P. Furgale, "Keyframe-based visual-inertial odometry using nonlinear optimization," *The International Journal of Robotics Research*, vol. 34, no. 3, pp. 314–334, 2015.
- [6] P. J. Besl and N. D. McKay, "A method for registration of 3-d shapes," *IEEE Transactions on Pattern Analysis and Machine Intelligence*, vol. 14, no. 2, pp. 239–256, 1992.
- [7] A. Segal, D. Haehnel, and S. Thrun, "Generalized-icp," in *Robotics: science and systems*, vol. 2, no. 4. Seattle, WA, 2009, p. 435.
- [8] T. Stoyanov, M. Magnusson, H. Andreasson, and A. J. Lilienthal, "Fast and accurate scan registration through minimization of the distance between compact 3d ndt representations," *The International Journal of Robotics Research*, vol. 31, no. 12, pp. 1377–1393, 2012.
- [9] J. Behley and C. Stachniss, "Efficient surfel-based slam using 3d laser range data in urban environments," in *Robotics: Science and Systems*, 2018.
- [10] J. Zhang and S. Singh, "Loam: Lidar odometry and mapping in real-time," in *Robotics: Science and Systems Conference (RSS)*, Berkeley, CA, Jul. 2014.
- [11] T. Shan and B. Englot, "Lego-loam: Lightweight and ground-optimized lidar odometry and mapping on variable terrain," in *IEEE/RSJ International Conference on Intelligent Robots and Systems (IROS)*. IEEE, 2018, pp. 4758–4765.
- [12] J. Lin and F. Zhang, "Loam_livox: A fast, robust, high-precision LiDAR odometry and mapping package for LiDARs of small FoV," *arXiv e-prints*, p. arXiv:1909.06700, Sep. 2019.
- [13] J. Zhang, M. Kaess, and S. Singh, "On degeneracy of optimization-based state estimation problems," in *2016 IEEE International Conference on Robotics and Automation (ICRA)*. IEEE, 2016, pp. 809–816.
- [14] G. Blais and M. D. Levine, "Registering multiview range data to create 3d computer objects," *IEEE Transactions on Pattern Analysis and Machine Intelligence*, vol. 17, no. 8, pp. 820–824, 1995.
- [15] R. Benjema and F. Schmitt, "A solution for the registration of multiple 3d point sets using unit quaternions," in *European Conference on Computer Vision*. Springer, 1998, pp. 34–50.
- [16] P. J. Neugebauer, "Reconstruction of real-world objects via simultaneous registration and robust combination of multiple range images," *International journal of shape modeling*, vol. 3, no. 01n02, pp. 71–90, 1997.
- [17] R. Bergevin, M. Soucy, H. Gagnon, and D. Laurendeau, "Towards a general multi-view registration technique," *IEEE Transactions on Pattern Analysis and Machine Intelligence*, vol. 18, no. 5, pp. 540–547, 1996.
- [18] F. Lu and E. Milios, "Globally consistent range scan alignment for environment mapping," *Autonomous robots*, vol. 4, no. 4, pp. 333–349, 1997.
- [19] K. Pulli, "Multiview registration for large data sets," in *Second International Conference on 3-D Digital Imaging and Modeling (Cat. No. PR00062)*. IEEE, 1999, pp. 160–168.
- [20] D. F. Huber and M. Hebert, "Fully automatic registration of multiple 3d data sets," *Image and Vision Computing*, vol. 21, no. 7, pp. 637–650, 2003.
- [21] D. Borrmann, J. Elseberg, K. Lingemann, A. Nüchter, and J. Hertzberg, "Globally consistent 3d mapping with scan matching," *Robotics and Autonomous Systems*, vol. 56, no. 2, pp. 130–142, 2008.
- [22] G. Grisetti, R. Kümmerle, C. Stachniss, and W. Burgard, "A tutorial on graph-based slam," *IEEE Intelligent Transportation Systems Magazine*, vol. 2, no. 4, pp. 31–43, 2010.
- [23] E. Mendes, P. Koch, and S. Lacroix, "Icp-based pose-graph slam," in *2016 IEEE International Symposium on Safety, Security, and Rescue Robotics (SSRR)*, 2016, pp. 195–200.
- [24] Y. Tsin and T. Kanade, "A correlation-based approach to robust point set registration," in *European conference on computer vision*. Springer, 2004, pp. 558–569.
- [25] E. B. Olson, "Real-time correlative scan matching," in *2009 IEEE International Conference on Robotics and Automation*. IEEE, 2009, pp. 4387–4393.
- [26] W. Maddern, A. Harrison, and P. Newman, "Lost in translation (and rotation): Rapid extrinsic calibration for 2d and 3d lidars," in *2012 IEEE International Conference on Robotics and Automation*. IEEE, 2012, pp. 3096–3102.
- [27] G. Ferrer, "Eigen-factors: Plane estimation for multi-frame and time-continuous point cloud alignment," in *IROS*, 2019, pp. 1278–1284.
- [28] H. Ye, Y. Chen, and M. Liu, "Tightly coupled 3d lidar inertial odometry and mapping," in *2019 International Conference on Robotics and Automation (ICRA)*. IEEE, 2019, pp. 3144–3150.
- [29] H. Surmann, A. Nüchter, and J. Hertzberg, "An autonomous mobile robot with a 3d laser range finder for 3d exploration and digitalization of indoor environments," *Robotics and Autonomous Systems*, vol. 45, no. 3–4, pp. 181–198, 2003.
- [30] D. Droschel and S. Behnke, "Efficient continuous-time slam for 3d lidar-based online mapping," in *2018 IEEE International Conference on Robotics and Automation (ICRA)*. IEEE, 2018, pp. 1–9.
- [31] D. Hähnel, W. Burgard, and S. Thrun, "Learning compact 3d models of indoor and outdoor environments with a mobile robot," *Robotics and Autonomous Systems*, vol. 44, no. 1, pp. 15–27, 2003.
- [32] C. Hertzberg, R. Wagner, U. Frese, and L. Schröder, "Integrating generic sensor fusion algorithms with sound state representations through encapsulation of manifolds," *Information Fusion*, vol. 14, no. 1, pp. 57–77, 2013.
- [33] J. J. Moré, *The Levenberg-Marquardt algorithm: implementation and theory*. Springer, 1978.
- [34] J. Lin and F. Zhang, "A fast, complete, point cloud based loop closure for lidar odometry and mapping," *arXiv preprint arXiv:1909.11811*, 2019.
- [35] M. Quigley, K. Conley, B. Gerkey, J. Faust, T. Foote, J. Leibs, R. Wheeler, and A. Ng, "Ros: an open-source robot operating system," in *ICRA Workshop on Open Source Software*, vol. 3, 01 2009.
- [36] R. B. Rusu and S. Cousins, "3d is here: Point cloud library (pcl)," in *2011 IEEE International Conference on Robotics and Automation*, 2011, pp. 1–4.